Eddy covariance observations of surface leakage during shallow subsurface CO_2 releases

Jennifer L. Lewicki[1*], George E. Hilley[2], Marc L. Fischer[3], Lehua Pan[1], Curtis M. Oldenburg[1], Laura Dobeck[4], Lee Spangler[4]

[1*]Earth Sciences Division, Ernest Orlando Lawrence Berkeley National Laboratory, 1 Cyclotron Rd., Berkeley, CA, 94720 USA, e-mail: jllewicki@lbl.gov, ph: 510-495-2818, fax: 510-486-5686

[2]Department of Geological and Environmental Sciences, Stanford University, Stanford, CA, 94305 USA

[3]Environmental Energy Technology Division, Ernest Orlando Lawrence Berkeley National Laboratory, 1 Cyclotron Rd., Berkeley, CA, 94720 USA

[4]Department of Chemistry and Biochemistry, Montana State University, 108 Gaines Hall, PO Box 173400, Bozeman, MT, 59717 USA

Abstract. We tested the ability of eddy covariance (EC) to detect, locate, and quantify surface CO_2 flux leakage signals within a background ecosystem. For 10 days starting on 07/09/2007, and for seven days starting on 08/03/2007, 0.1 (Release 1) and 0.3 (Release 2) t CO_2 d^{-1}, respectively, were released from a horizontal well ~100 m in length and ~2.5 m in depth located in an agricultural field in Bozeman, MT. An EC station measured net CO_2 flux (F_c) from 06/08/2006 to 09/04/2006 (mean and standard deviation = -12.4 and 28.1 g m^{-2} d^{-1}, respectively) and from 05/28/2007 to 09/04/2007 (mean and standard deviation = -12.0 and 28.1 g m^{-2} d^{-1}, respectively). The Release 2 leakage signal was visible in the F_c time series, whereas the Release 1 signal was difficult to detect within variability of ecosystem fluxes. To improve detection ability, we calculated residual fluxes (F_{cr}) by subtracting fluxes corresponding to a model for net ecosystem exchange from F_c. F_{cr} had reduced variability and lacked the negative bias seen in corresponding F_c distributions. Plotting the upper 90th percentile F_{cr} versus time enhanced the Release 2 leakage signal. However, values measured during Release 1 fell within the variability assumed to be related to unmodeled natural processes. F_{cr} measurements and corresponding footprint functions were inverted using a least-squares approach to infer the spatial distribution of surface CO_2 fluxes during Release 2. When combined with flux source area evaluation, inversion results roughly located the CO_2 leak, while resolution was insufficient to quantify leakage rate.

Keywords: Eddy covariance; Carbon dioxide flux; Geologic carbon storage monitoring; Leakage; Accumulation chamber method

1. Introduction

One approach being considered to help mitigate rising atmospheric CO_2 concentrations is geologic carbon sequestration (GCS) [e.g., *International Energy Agency*, 1997, 2004; *IPCC*, 2005]. The possibility of leakage of CO_2 from underground storage sites along permeable pathways such as well bores or faults is a primary concern for the safety and effectiveness of GCS. Should it occur, this leakage could have harmful effects on the near-surface environment. Therefore, in addition to CO_2 capture, transportation, and injection technology, GCS requires monitoring approaches with the ability to detect, locate, and quantify potential CO_2 leakage in the near-surface environment.

While numerous techniques are available to measure CO_2 concentrations and fluxes within the near-surface environment, detection and characterization of potential CO_2 leakage from geologic storage reservoirs will pose a challenge due to the large spatial and temporal variation in background CO_2 fluxes [e.g., *Lewicki et al.,* 2005; *Cortis et al.,* 2008]. Eddy covariance (EC) is a micrometeorological approach traditionally used to measure trace gas and heat fluxes across the interface between the atmosphere and a plant canopy under certain atmospheric and terrain conditions [e.g., *Baldocchi*, 2003]. EC offers the benefit of an automated flux measurement that does not interfere with the ground surface and is averaged over both time and space, with the spatial scale significantly larger (m^2-km^2) than that of many other ground-based techniques. For these reasons, EC has been proposed for use in GCS monitoring programs [e.g., *Oldenburg et al.*, 2003; *Miles et al.*, 2005; *Benson*, 2006; *Leuning et al.,* 2008]. Several studies have

used EC to measure artificial tracers released at the surface in simple geometric configurations to verify footprint models [e.g., *Foken and Leclerc*, 2004 and references therein]. EC has also been shown to provide reliable measurements of relatively large-magnitude volcanic CO_2 fluxes resulting from gas migration from natural geologic reservoirs to the surface [*Anderson and Farrar*, 2001; *Werner et al*., 2000; 2003; *Lewicki et al.*, 2008]. However, the ability of EC to detect, locate, and quantify potentially small subsurface-derived CO_2 leakage signals within the large background variability of ecological fluxes is largely untested.

A facility was recently built in an agricultural field at Montana State University by the Zero Emissions Research and Technology (ZERT) Project, where CO_2 can be released into the shallow subsurface from point and line sources that emulate leakage along, e.g., abandoned wells or faults [*Lewicki et al.*, 2007]. In July and August 2007, two controlled releases of CO_2 were carried out at different rates from a shallow horizontal well; the spatio-temporal evolution of surface leakage signals was characterized by repeated measurements of soil CO_2 flux using the accumulation chamber method [*Lewicki et al.,* 2007]. In this study, we deployed an EC station in the field from 06/08/2006 to 09/04/2006 and from 05/28/2007 to 09/04/2007, which allowed us to establish a baseline of background summertime net CO_2 flux variability for the study site. To improve our ability to detect CO_2 leakage, we apply a filter to the time series that removes the ecological CO_2 flux signal that is correlated with changes in intensity of light and soil temperature. Once leakage is detected, we use least-squares inversions of measured EC CO_2 fluxes and modeled footprint functions to roughly locate and image the geometry of

the surface CO_2 leak. To our knowledge, this represents the first time that such inversions of EC measurements have been used to model the spatial distribution of heterogeneous surface CO_2 fluxes. Our results suggest that under careful, site-specific experiment design, EC is a promising tool to detect and locate leakage signals of moderate to high magnitude and/or spatial extent, while detection of relatively small leakage signals may require the use of alternative measurement approaches.

2. Field Site and CO_2 Release Experiments

The CO_2 release experiments were conducted at Montana State University, at the Montana Agricultural Experiment Research Center in Bozeman, MT (45°39'N, 111°04'W). The study site was a ~0.12 km^2, nearly flat field, with vegetation composed primarily of prairie grasses, alfalfa, and Canadian thistle. The field was mowed/hayed on 11 July 2006 and then on 22 June 2007. While leaf area index was not measured in this study, it would have been greatly reduced when the field was mowed, thus reducing plant photosynthetic uptake of CO_2. A ~0.2 to 1.2 m-thick clay topsoil here overlies an alluvial sandy cobble. A well, oriented 45° to the northeast, was installed in the field using horizontal drilling in December 2006. This well had a 70-m long perforated and nearly-horizontal section at its center and unperforated sections on its two sloping ends (Figure 1). The perforated section was located at ~1.3-2.5 m depth, sub-water table, within the alluvial sandy cobble and was divided into six zones separated by 0.4-m wide inflatable packers. Five zones were 12 m in length and one zone (on the far southwest end of the well) was 9 m in length. When inflated, the packers prevented fluid flow between the six

perforated well zones. Packer inflation and CO_2 delivery lines were installed in the well to flow air to the packers and CO_2 to each of the six perforated well zones, respectively. Because horizontal drilling was used to install the well, the original soil profile and vegetation over the well were minimally disturbed. From 9-18 July 2007, 0.1 t CO_2 d^{-1} (100 kg CO_2 d^{-1}) were released from the well, 13.0 kg CO_2 d^{-1} from the far southwest perforated zone and 17.4 kg CO_2 d^{-1} from each of the other five zones (hereafter referred to as Release 1). This rate was chosen based on numerical simulations to provide a challenging detection problem while still ensuring that injected CO_2 would reach the ground surface. Then, from 3-10 August 2007, 0.3 t CO_2 d^{-1} (300 kg CO_2 d^{-1}) were released (hereafter referred to as Release 2). This rate was chosen to obtain a larger surface flux for demonstration purposes. CO_2 flow rate to, and pressure within each of the perforated well zones were monitored during the releases.

Lewicki et al. [2007] measured soil CO_2 flux repeatedly on a daily basis from 7-18 July and from 7-12 August 2007 using the accumulation chamber method [e.g., *Chiodini et al.*, 1998]. An opaque chamber was used and vegetation within the chamber footprint area was clipped so that only soil CO_2 efflux (ecosystem respiration + leakage) was measured. Figure 2 shows contour maps of soil CO_2 flux measured prior to Release 1, on Day 8 of Release 1, and on Day 8 of Release 2. Surface CO_2 leakage occurred during both releases at 5-6 points aligned along surface trace of the well (Figure 2 b and c). The maximum soil CO_2 flux measured during Release 1 was high, ~1600 g $m^{-2}d^{-1}$ (~420 µmol m^{-2} s^{-1}) relative to background ecosystem respiration fluxes; however, the total CO_2 release rate of 0.1 t d^{-1} was of similar magnitude as background ecosystem respiration

flux integrated over the relatively small grid area (7.7 x 10^3 m^2) [*Lewicki et al.,* 2007]. Leakage fluxes measured during Release 2 along the well trace increased (up to 6000 g m^{-2} d^{-1}) relative to Release 1 and the total CO_2 release rate of 0.3 t d^{-1} was approximately three times that of background ecosystem respiration flux integrated over the grid area at that time. Further details of soil CO_2 flux measurements and the relationship of surface CO_2 leakage flux distribution to the well design are found in *Lewicki et al.* [2007].

3. Measurement of EC Net CO_2 Flux and Environmental Parameters

An EC station was deployed near the center of the field from 8 June to 4 September 2006 and then 27 m northwest of the release well from 28 May to 4 September 2007 (Figure 2a). The location of the station was chosen to take advantage of east-southeasterly prevailing winds, which would frequently situate the EC station downwind of the well leakage source (Section 4.1). The station was similar in design to that described by *Billesbach et al.* [2004] and was composed of fast- and slow-response subsystems. The fast-response subsystem included two sensors used to measure the variables necessary to calculate turbulent fluxes of CO_2, H_2O, heat, and momentum. A Gill-Solent WindMaster Pro sonic three-dimensional anemometer/thermometer (Gill Instruments, Ltd) measured wind speeds in three orthogonal directions and sonic temperature at 10 Hz. A LI-COR 7500 open-path CO_2-H_2O infrared gas analyzer (LI-COR, Inc) measured CO_2 and water vapor densities at 10 Hz. Both sensors were mounted atop a tripod tower at 3.2 m height from 8 June to 4 September 2006, 3.0 m height from 28 May to 18 July 2007, and 2.8 m height from 19 July to 4 September 2007.

The slow-response subsystem included sensors (Table 1) associated with a second tripod tower that measured auxiliary meteorological and soil physical parameters. Radiation sensors were mounted to a horizontal bar extending from the tripod tower at 2 m height. Soil moisture profiles (10 and 30 cm depth) were measured at two locations. Since the soil moisture probes were not calibrated for the soil at the study site, we refer to measurements as "relative soil moisture", and only assess the data qualitatively. Soil temperature profiles (10, 20, and 30 cm depth) were measured at two locations. Soil heat flux was measured at four locations at 5 cm depth near the radiometer. Slow-response subsystem variables were measured every 5 seconds and averaged over 30 minutes for comparison with turbulent fluxes.

Net CO_2 flux (F_c) was calculated as the temporal covariance of CO_2 density (c) and vertical wind velocity (w):

$$F_c = \overline{w'c'} \qquad (1)$$

where the overbar denotes time averaging and primes denote fluctuations in w and c relative to their mean values. Fluxes were calculated for 30-minute periods. Equation 1 gives the mean vertical turbulent flux of CO_2 over a horizontally homogeneous surface under steady-state conditions. The lower measurement detection limit is estimated to be 2 g m^{-2} d^{-1} over relatively short vegetation when ecosystem F_c is relatively high. For each half-hour of data, the mean lateral ($\overline{v}$) and then the mean vertical ($\overline{w}$) wind velocities

were rotated to zero [*Kaimal and Finnigan,* 1994]. The WPL correction for the effects of fluctuation in heat and water vapor on the density of air [*Webb et al.,* 1980] was applied. Raw signals from the infrared gas analyzer and sonic anemometer were evaluated for spikes and all points more than ten standard deviations (thereby accepting a non-Gaussian tail to the data) away from a 600 s moving average were removed from the data; gaps were then filled using a 10 s moving average. Turbulent fluxes measured during the nighttime under low turbulent conditions can be systematically underestimated [e.g., *Aubinet et al.,* 2000; *Massman and Lee,* 2002]. Supplement 1 shows a plot of F_c versus friction velocity (u_*), calculated as the square root of the momentum flux, for nighttime EC measurements made in 2006 and 2007, excluding data collected during Releases 1 and 2, the week following mowing of the field in 2006, and the week following mowing of the field in 2007. We chose two u_* thresholds (0.15 and 0.23 m s^{-1}) below which nighttime F_c was discarded in 2006 and 2007 time series to compare their effects on loss of underestimated fluxes. Because nighttime half-hour and average-daily F_c measured in 2006 and 2007 were similar for $u_* > 0.15$ and $u_* > 0.23$ m s^{-1} thresholds (Supplement 2) and the 0.15 m s^{-1}threshold allowed us to retain a larger number of data for further analysis and modeling of ecosystem CO_2 fluxes (Section 4.2), we discarded nighttime F_c data corresponding to $u_* \leq 0.15$ m s^{-1}. Data were tested for stationarity according to *Foken and Wichura* [1996]. Each 30-minute F_c measurement was divided into six five-minute segments. If the difference between the average of the five-minute segments and the 30-minute measurement was greater than 30%, then the measurement was considered non-stationary and discarded. Based on filtering F_c time series for u_* and stationarity criteria, 43 and 50% of data points were rejected in 2006 and 2007, respectively.

4. Results

4.1. Meteorology

Winds were primarily either from the east-southeast or from the northwest, with the highest wind speeds measured typically from easterly directions (Figure 3). Figure 4 shows average daily atmospheric temperature, vapor pressure deficit (VPD), PAR, and relative soil moisture and daily cumulative precipitation measured in 2006 and 2007. Average summertime (June-August) atmospheric temperatures were comparable for 2006 and 2007 (~18^{o}C), with maximum average daily values observed in July (Figure 4a and d). Cumulative summertime rainfall was 118.4 mm in 2006; neglecting the week of data loss in July 2007, it was 43.9 mm over the same timeframe in 2007 (Figure 4c and f). The highest summertime rainfall occurred in June of 2006 and 2007. In July-August 2007, daily cumulative precipitation exceeded ~1 mm on only three days, which occurred either during or several days prior to Releases 1 and 2 (Figure 4f). The rain during Release 2 on 6 August 2007 was associated with a decrease in both atmospheric temperature and VPD. Average daily relative soil moisture showed a long-term decline over the summers of 2006 and 2007, with shorter-term increases observed associated with heavy rain events (Figure 4b and e).

4.2. Detection of CO_2 leakage signal within ecosystem variability

The 2006 and 2007 F_c time series are shown in Figure 5. Data gaps were caused by loss of power, intense precipitation events, or filtering with respect to $u*$ and non-stationarity. Based on these data, the field was a net sink for CO_2 prior to mowing in both 2006 and 2007. After mowing, the field rapidly became a net source for CO_2 when plant leaf area and photosynthetic uptake were dramatically decreased. Daytime CO_2 uptake then gradually increased through late July/early August, thereafter remaining relatively constant for the remainder of the 2006 and 2007 observation periods. CO_2 leakage during Release 1 was not possible to detect within the large background variability of the F_c time series (Figure 5b). F_c values measured during Release 2 showed a positive shift upwards, relative to the weeks prior to and following the release. The mean and standard deviation of the 2006 F_c time series were -12.4 and 28.1 g m^{-2} d^{-1}, respectively (Figure 6a), whereas the mean and standard deviation of the 2007 F_c time series were -12.0 and 28.1 g m^{-2} d^{-1}, respectively (Figure 6b).

As observed, the large variability of ecosystem fluxes can mask CO_2 leakage signals similar to those studied here, particularly if we lack a priori knowledge of the location of the leakage source. While the location of the leakage source was known in this study, this will not necessarily be the case at many GCS sites where monitoring for potential CO_2 leakage is carried out. Consequently, we chose not to filter F_c data for wind direction (i.e., eliminate data corresponding to times when the EC station was located upwind of the well). Estimation and removal of the contribution of net ecosystem exchange (*NEE*) from the total measured flux, F_c may instead improve our ability to detect leakage at many sites. *NEE* can be partitioned into photosynthetic uptake by the plant canopy and

ecosystem respiration from plants and soil. These constituent fluxes are influenced by a broad range of factors such as meteorology, soil physical and chemical properties, and plant functional and structural characteristics. However, intensity of light and soil temperature are strong drivers of short time-scale variations in plant photosynthetic uptake and ecosystem respiration, respectively. As a result, empirically derived relationships between these environmental parameters and F_c have been used to decompose F_c into respiration and photosynthetic flux components and gap-fill F_c time series [e.g., *Aubinet et al*., 2000; *Falge et al.,* 2001; *Reichstein et al.,* 2005; *Fischer et al.*, 2007]. Here, we estimate the ecological F_c signals correlated with changes in light and soil temperature and remove them from the 2006 and 2007 F_c time series.

We use a rectangular hyperbolic function [e.g., *Falge et al.*, 2001] to describe *NEE* in terms of photosynthetic uptake and respiratory release of CO_2:

$$NEE = -\left(\frac{F_{\max}\alpha PAR}{\alpha PAR + F_{\max}}\right) + R_{eco} \qquad (2)$$

where F_{max} is the maximum CO_2 flux at infinite light, α is the apparent quantum yield, and R_{eco} is the respiration CO_2 flux from plants and soil. Substituting an exponential function that describes the relationship between soil temperature (T_{soil}) and R_{eco} [*Lloyd and Taylor*, 1994] into equation (2) yields:

$$NEE = -\left(\frac{F_{\max}\alpha PAR}{\alpha PAR + F_{\max}}\right) + b_0 \exp(bT_{soil}) \qquad (3)$$

where b and b_0 are empirical coefficients. Using nonlinear optimization methods, equation (3) was fit to half-hour F_c, T_{soil} (20 cm depth), and PAR data for three-day moving (half-hour time step) windows through the entire 2006 and 2007 measurement periods to estimate α, F_{max}, b and b_0 parameters for the center point in the moving window. Predicted values of *NEE* were then calculated for the center point based on measured F_c, T_{soil}, and PAR values and best-fit parameters. We required a minimum of 20 data points within the three-day moving window for estimation of α, F_{max}, b and b_0. If fewer data points were present within the window for a given time step, then a gap occurred for predicted *NEE*. Supplement 3 shows RMS errors as the misfit between predicted *NEE* and F_c for the three-day moving windows versus time for 2006 and 2007 time series.

Residual F_c (F_{cr}) was calculated by subtracting predicted *NEE* from measured F_c. This simple "ecological flux filter" only reduces fluctuations in F_c that are correlated with variations in T_{soil} and light. The filter does not account for fluctuations in F_c that may be related to variations in, for example, soil moisture, litter, and perhaps even photosynthetic uptake associated with elevated atmospheric CO_2 concentrations during a leak. Consequently, F_{cr} values represent our best estimate of fluxes that may result from unmodeled natural processes, background instrument noise, and the CO_2 leak of interest. F_{cr} for 2006 and 2007 time series were normally distributed and nearly unbiased (Figure 6c and d), with 2006 mean and standard deviation = 0.0 and 8.1 g m^{-2} d^{-1}, respectively, and 2007 mean and standard deviation = -0.1 and 9.3 g m^{-2} d^{-1}, respectively. Since we

expect a CO_2 leakage flux signal to be expressed more strongly in the upper tail of a F_{cr} distribution, we isolated the upper 90th percentile F_{cr} to identify points that may be indicative of leakage. A cumulative distribution function of F_{cr} was calculated for a seven-day moving window (advancing in half-hour time steps) and the upper 90th percentile flux of that distribution was assigned to center point of the window. The time series of these upper 90th percentile F_{cr} values for 2006 and 2007 are shown in Figure 7. For a stationary Gaussian distribution, the upper 90th percentile F_{cr} is 1.3 standard deviations above the mean. Assuming stationarity and that the mean is zero for 2006 and 2007 F_{cr} distributions, the upper 90th percentile F_{cr} for these distributions = 10.5 and 12.1 g m^{-2} d^{-1}, respectively. These values are shown as the dashed horizontal lines on Figure 7. With the exception of several high-frequency increases in the upper 90th percentile F_{cr} values near the beginning of the 2006 and 2007 observation periods, and the longer-lived, relatively high values observed during Release 2, upper 90th percentile F_{cr} lie close to or below those expected from random sampling a normal distribution. Upper 90th percentile F_{cr} observed near the timing of 2006 and 2007 mowing are close to the 10.5 and 12.1 g m^{-2} d^{1} thresholds, respectively. While upper 90th percentile F_{cr} observed during Release 1 lie within the variability of background values, those measured during Release 2 are highly anomalous and sustained over multiple days (Figure 7).

4.4. Location and quantification of CO_2 leakage signal

After CO_2 leakage was detected during Release 2, we used a radial plot of F_{cr} as a function of mean horizontal wind direction (Figure 8) to determine the direction from

which the leakage signal was derived. Figure 8 shows F_{cr} color coded for measurement time, where the relatively large orange dots with black outlines were measured during Release 2. If we assume that $F_{cr} > 18$ g m^{-2} d^{-1} is anomalously high (greater than ~ two standard deviations above the mean), then 19 anomalously high values were measured during Release 2, while 68 were measured during the entire 2007 observation period. Since 28% of anomalously high F_{cr} values were measured during Release 2 and the release only lasted for 8% of the 2007 observation period, anomalously high F_{cr} are more than three times over-represented during Release 2, relative to the rest of the observation period. Anomalously high F_{cr} values were typically measured during Release 2 when the EC station was downwind of the release well (mean horizontal wind direction between 45 and 225^{o}; Figure 8).

The F_c measured by EC at a point (x_m, y_m, z_m) is representative of the weighted average of the upwind surface CO_2 emissions. The influence of each surface point source emission on F_c depends on its location relative to the EC sensors. F_c is related to the distribution of source CO_2 fluxes (Q_c) at the surface (x', y', $z' = z_0$) determined by the footprint or source weight function, $f(x_m - x',\ y_m - y',\ z_m - z_0)$:

$$F_c(x_m, y_m, z_m) = \int_{-\infty}^{\infty}\int_{-\infty}^{\infty} Q_c(x', y', z' = z_0) \cdot f(x_m - x', y_m - y', z_m - z_0)\,dx'dy' \qquad (4)$$

[e.g., *Horst and Weil*, 1992; *Schmid*, 1997]. The footprint function varies with factors such as EC sensor height, atmospheric stability, and surface roughness; however, the value (weight) of the footprint function generally rises to a maximum some distance

upwind of the EC sensors, then smoothly falls off in all directions. The total surface influence on F_c, or the source area, is the integral beneath the footprint function. Should the spatial distribution of Q_c remain constant over time, changes in F_c will reveal this distribution as the footprint function varies with atmospheric conditions. Thus, in principle, it should be possible to infer the spatial distribution of Q_c using a number of F_c measurements that source different areas, with the purpose of locating and quantifying a potential CO_2 leak [e.g., *Miles et al.,* 2005].

We attempt to infer the spatial distribution of surface fluxes during Release 2 using a linear, least-squares inversion [e.g., *Menke*, 1989] of 75 modeled footprint functions and F_{cr} observed during the release. This approach is similar to other geophysical inversions, such as geodetic inferences of fault slip rates based on surface deformations [e.g*., Harris and Segall*, 1987] or tomographic imaging of the seismic velocity structure of the earth based on multiple travel times of teleseismic waves [e.g., *Dahlen and Tromp*, 1998]. In this particular application, we note that the F_{cr} can be modeled as the weighted sum of the Q_c distribution from which ecological signals have been removed (Q_{cr}), hereafter approximated as unvarying in time. Thus, F_{cr} can be written as:

$$\overrightarrow{F_{cr}} = \hat{G}\overrightarrow{Q_{cr}} \tag{5}$$

where $\overrightarrow{F_{cr}}$ is a vector whose length is the number of observations collected during the release, and $\hat{G}$ is a matrix that contains the modeled footprint functions (f) that map the unknown surface fluxes ($\overrightarrow{Q_{cr}}$) into $\overrightarrow{F_{cr}}$. Given $\hat{G}$, we estimate the spatial distribution $\overrightarrow{Q_{cr}}$

that best explains the observed $\overrightarrow{F_{cr}}$. We use a least-squares solution to this problem, which allows us to write the unknown spatial distribution of surface fluxes in terms of $\overrightarrow{F_{cr}}$ and $\hat{G}$ as follows:

$$\overrightarrow{Q_{cr}} = (\hat{G}^T \hat{W} \hat{G})^{-1} \hat{G}^T \hat{W} \overrightarrow{F_{cr}} \qquad (6)$$

where $\hat{W}$ is the covariance matrix of the observed $\overrightarrow{F_{cr}}$, and $\hat{G}^T$ is the transpose of the data kernel. If we assume that fluctuations in $\overrightarrow{F_{cr}}$ are independent from one another, $\hat{W}$ reduces to a diagonal matrix whose dimensions are equal to the number of observations, and whose values are the inverse of the variance of the $\overrightarrow{F_{cr}}$ data (7.4×10^{-3} g^{-2} m^4 d^2). If many more observations of $\overrightarrow{F_{cr}}$ exist than there are unknown $\overrightarrow{Q_{cr}}$ values, then Equation 6 is sufficient to infer the spatial distribution of $\overrightarrow{Q_{cr}}$.

In the current study, there are more $\overrightarrow{Q_{cr}}$ values to be inferred than there are observations of $\overrightarrow{F_{cr}}$. In addition, when Equation 6 is applied to, for example, geodetic data, the best-fit solutions for $\overrightarrow{Q_{cr}}$ often vary abruptly in space and produce extremely rough solutions that are physically untenable [e.g., *Harris and Segall*, 1987]. For these reasons, following methods developed in the geodetic and seismological communities, we apply an additional constraint to the weighted least squares inversion that requires spatial continuity when finding the best-fit values for $\overrightarrow{Q_{cr}}$. This constraint requires the curvature in the values of $\overrightarrow{Q_{cr}}$ to be minimized between adjacent points while satisfying the observed $\overrightarrow{F_{cr}}$ values. This is accomplished by combining $\hat{G}$ with a second *m* x *m* matrix

(where *m* is the number of cells within which $\overrightarrow{Q_{cr}}$ is inferred), hereafter referred to as $\hat{G}_{sm}$. This matrix uses a finite difference expression to calculate curvature based on the inferred flux values at each grid point and those points directly adjacent to it within the inferred source area (assuming points outside of the source area have zero surface flux). In addition, a second vector (referred to as $\overrightarrow{F_{sm}}$) is combined with $\overrightarrow{F_{cr}}$; this vector's length is that of $\overrightarrow{Q_{cr}}$, and its values are set to zero to minimize the curvature of $\overrightarrow{Q_{cr}}$. By combining $\hat{G}$ with $\hat{G}_{sm}$, $\overrightarrow{F_{cr}}$ with $\overrightarrow{F_{sm}}$, and applying Equation 6, the values of $\overrightarrow{Q_{cr}}$ will reflect a compromise between the surface flux values inferred from $\overrightarrow{F_{cr}}$ and the requirement of smoothness across the solution space. This has the effect of overly smoothing $\overrightarrow{Q_{cr}}$ in areas that are poorly defined by the observed $\overrightarrow{F_{cr}}$ values, while honoring $\overrightarrow{Q_{cr}}$ in areas well defined by the observed data.

The distribution of $\overrightarrow{Q_{cr}}$ inferred from this method represents a compromise between the constraints provided by observations versus those that require a spatially smooth solution. The relative influence of these two sets of constraints is controlled by specifying the weight that the smoothing function receives in the solution relative to the observations, which we refer to as w_{sm}. When w_{sm} is set to a large value, the smoothness of modeled $\overrightarrow{Q_{cr}}$ will be favored over the fit between measured and modeled $\overrightarrow{F_{cr}}$. However, when w_{sm} is set to a small value, the solution will become rougher and more poorly defined for many values of $\overrightarrow{Q_{cr}}$, while the fit between measured and modeled $\overrightarrow{F_{cr}}$ will improve. As is customary in the geophysical literature [e.g., *Harris and Segall*, 1987], for different w_{sm}

we plot the misfit between measured and modeled $\overrightarrow{F_{cr}}$ (as the weighted residual sum of squares; WRSS) versus roughness of $\overrightarrow{Q_{cr}}$:

$$roughness = \sum_{i=1}^{m} \left(Q_{cr,i} - \overline{Q_{cr}} \right)^2 \quad (7)$$

By systematically changing the value of w_{sm}, we can determine values of this parameter that result in the greatest decrease in the solution roughness that does not necessitate a correspondingly large change in the data misfit. Thus, we use this plot to identify the optimal w_{sm} that produces a reasonably smooth model result and maintains an acceptable level of misfit.

To model $\overrightarrow{Q_{cr}}$, we discretized the surface surrounding the EC station into an 800 m x 800 m solution domain. The linear dimension of each square pixel for which $\overrightarrow{Q_{cr}}$ was determined was equal to 10 m. The Flux Source Area Model (FSAM) of *Schmid* [1997], based on analytic solutions of the advection-diffusion equation [*Horst and Weil*, 1992] was used to model footprint functions using the following inputs: (1) z_m = 2.8 m; (2) surface roughness height, z_0 = 0.05 m, based on vegetation height measured during Release 2; (3) measured mean horizontal wind direction; (4) cross-wind turbulence near the surface characterized by calculated σ_v/u_*, where σ_v is the standard deviation of the wind speed in the cross-wind direction; (5) calculated Monin-Obukhov length, L (Supplement 4). We calculated f at the center of each 10 m x 10 m pixel. Since the source area here was defined as the area from which 90% of the $\overrightarrow{F_{cr}}$ was derived, we

renormalized *f* to reflect this partial sampling by the model. $\overrightarrow{F_{cr}}$ values corresponding to source areas greater than the 0.64 km^2 area of the model domain and/or footprint models that did not converge were not considered in the inversion.

Figure 9 shows a plot of the misfit between measured and modeled $\overrightarrow{F_{cr}}$ (WRSS) versus $\overrightarrow{Q_{cr}}$ roughness. A smoothing weight of $10^{-8.5}$ was selected for the model inversion, which provided the optimal compromise between spatial continuity across the model solution space and misfit between measured and modeled $\overrightarrow{F_{cr}}$. Inversion results are shown in Figure 10 for a 400 x 400 m area to highlight the region close to the EC station. Results for the full 800 x 800 m model domain are given in Supplement 5. The inversion results show large-scale areas of relatively high $\overrightarrow{Q_{cr}}$ values located at distances greater than ~75 m from, and to the NE and SW of the EC station (Figure 10a). A smaller area of positive $\overrightarrow{Q_{cr}}$ values was modeled closer to and southeast of the EC station. Based on the footprint function, only surface fluxes located upwind of the EC station will contribute to F_{cr}. Also, surface fluxes located far away from the EC station will tend to contribute a lesser extent to F_{cr} than those located in relatively close proximity. Thus, in minimizing the misfit, the model tends to push extreme flux values into portions of the solution domain for which the EC measurements provide little constraint. We constructed a contour map of the sum of footprint weights based on the 75 modeled footprint functions (Figure 10b), the "footprint climatology" [e.g., *Amiro*, 1998; *Göckede et al.,* 2008]. This map highlights those portions of the solution space that were well defined by the EC measurements and provides a qualitative assessment of the relative uncertainty of the model inversion results. Surface areas located within ~50 m of the EC station were

weighted most highly in modeled footprint functions; $\overrightarrow{Q_{cr}}$ values modeled within those regions were therefore well defined by EC measurements and associated with the greatest certainty. Surface fluxes located greater than ~ 75 m from the EC station were poorly resolved by EC measurements; smoothing thus dominates inversion results in these regions. Figure 10c shows the map of modeled $\overrightarrow{Q_{cr}}$ values, shaded for relative uncertainty so that $\overrightarrow{Q_{cr}}$ values that are not resolved by observations are masked. An area of relatively high $\overrightarrow{Q_{cr}}$ is located within ~30 m and southeast of the EC station. While the shape of this region is less elongate than the surface CO_2 flux leakage signal measured during Release 2 (Figure 10d), its location relative to the EC station is similar. Importantly, the central portion of the linear surface CO_2 flux leakage signal in Figure 10d is located in an area of greater footprint weight (Figure 10b) than the two ends of the signal. For comparison, Supplement 5 shows maps of $\overrightarrow{Q_{cr}}$, modeled using w_{sm} values of 10^{-13}, $10^{-8.5}$, and 10^{-4}. The area of relatively high $\overrightarrow{Q_{cr}}$ located within ~30 m and southeast of the EC station is consistent for all three inversions, while those areas defined only by smoothing vary strongly with w_{sm}.

To test our ability to quantify the surface leakage rate associated with Release 2 based on modeled $\overrightarrow{Q_{cr}}$, we integrated $\overrightarrow{Q_{cr}}$ values over the area of the accumulation chamber measurement grid (Figures 2 and 10d), which yielded CO_2 discharge = 0.02 t d^{-1}. Based on accumulation chamber measurements, *Lewicki et al.* [2007] estimated a leakage CO_2 discharge on Day 8 of Release 2 = 0.33 t d^{-1}. Assuming that the surface leakage CO_2 discharge was equal to the CO_2 release rate during Release 2 (0.3 t d^{-1}), accumulation

chamber measurements recorded 110% of the surface leakage rate, while EC measurements, based on modeled $\overrightarrow{Q_{cr}}$, recorded 7% of the surface leakage rate.

5. Discussion and Conclusions

The CO_2 release rates of Releases 1 and 2 and their associated surface leakage signals provided a challenge for detection of CO_2 leakage by EC. For example, the surface CO_2 leakage rate measured using the accumulation chamber method during Release 1 was less than or similar to the background ecosystem respiration flux integrated over the relatively small measurement grid area [*Lewicki et al.,* 2007]. Also, both releases resulted in surface CO_2 flux leakage signals of small spatial extent, relative to the EC flux source areas.

Measurements of F_c made during Summer 2006 and prior to Release 1 in 2007 allowed us to establish a baseline of background summertime variability for the study site. We first examined the raw 2007 F_c time series (Figure 5b) to assess whether CO_2 leakage signals associated with Releases 1 and 2 were possible to detect. No convincing change in F_c was discernable during the timeframe of Release 1, whereas a positive shift upwards in F_c was detectable during Release 2, relative to the week prior to and those following the release.

Removal of the ecosystem signal from the F_c time series that was correlated with changes in PAR and soil temperature greatly improved our ability to detect CO_2 leakage during Release 2. Application of this ecological flux filter reduced the variability of and

removed the negative bias from the 2006 and 2007 F_{cr} distributions, relative to the corresponding F_c distributions (Figure 6). Plotting the upper 90th percentile F_{cr} versus time (Figure 8) allowed us to isolate anomalously high residual fluxes associated with CO_2 leakage during Release 2. The 90th percentile F_{cr} values expected assuming stationary Gaussian distributions for 2006 and 2007 were similar (10.5 and 12.1 g m^{-2} d^{-1}, respectively), suggesting that similar factors controlled variability of the residuals during both years. These factors likely include the influence of fluctuations in VPD, precipitation, and soil moisture on F_c, other unmodeled natural processes, and to a lesser extent, EC instrument noise. Since the 2006 and 2007 F_{cr} distributions were not truly stationary, we observed variations in the upper 90th percentile F_{cr} away from the expected values. For example, the high frequency spikes in these values that occurred at the beginning of the 2006 and 2007 measurement periods are likely related to measurement noise during heavy precipitation events. Finally, while the CO_2 leakage signal associated with Release 2 emerged clearly in Figure 7, CO_2 leakage during Release 1 remained undetectable after the ecological F_c signal was removed. Detection of relatively small CO_2 leakage signals by EC will likely be difficult at many sites. However, if we are able to model and remove F_c signals associated with additional natural processes and instrument noise, detection ability may be improved.

Once a CO_2 leakage signal has been detected, EC may assist in its location and quantification when used in concert with other surface CO_2 flux measurement techniques. For example, we constructed a radial plot of F_{cr} as a function of wind direction (Figure 8), which confirmed that anomalously high F_{cr} values were measured during Release 2

typically when the EC station was downwind of the well leakage source. Without a priori knowledge of the leakage source location, such a radial plot could be used to estimate the direction from which CO_2 leakage is derived. EC footprint modeling would determine the approximate source areas from within which directionally consistent anomalously high F_{cr} values originate. A point CO_2 flux measurement approach such as the accumulation chamber method could then be used to locate and quantify CO_2 leakage [e.g., *Lewicki et al.,* 2007] within those areas.

Alternatively, EC has the potential to locate and quantify CO_2 leakage signals when used alone if (1) multiple EC stations are deployed in different locations or an array of EC sensors is installed at more than one height at a given location and simultaneously sample a leakage area with different flux footprints or (2) a leakage area is relatively stable over time and is sampled repeatedly by a single EC station with varying flux footprints. We showed that it was possible to locate a leakage signal with a location, geometry, and magnitude such as that of Release 2 using a single EC station by inversion of 75 F_{cr} measurements and corresponding footprint functions (Figure 10). To our knowledge, this is the first study to invert EC measurements to infer the spatial distribution of heterogeneous surface fluxes. Importantly, however, our map of modeled $\overrightarrow{Q_{cr}}$ only roughly resolved the location and geometry of the leakage signal, while the leakage rate was underestimated by ~93 %. Overall, the ability to locate, map the geometry of, and quantify a given CO_2 leakage signal using EC will be very challenging and depend on a wide range of factors, such as location of the EC sensors, magnitude, geometry, and spatio-temporal stability of the signal, atmospheric conditions at the time of the

measurements, surface roughness, site topography, and the number of EC measurements available for the inversion. Also, relatively high and heterogeneous CO_2 leakage emissions could potentially cause advection, leading to underestimation of the leakage signal by EC. In our case, the limited number of EC measurements available for inversion during the relatively short timeframe of Release 2 strongly impacted the resolution of modeled $\overrightarrow{Q_{cr}}$; a greater number of measurements would presumably improve the results. Furthermore, we showed that based on factors such as EC sensor location, site surface roughness, and atmospheric conditions, only the area within ~75 m of the EC station contributed substantially to F_c measurements (Figure 10b). Since the CO_2 leakage source was situated within this region, we were able to detect and locate it. In particular, the central part of the linear surface CO_2 flux leakage signal (Figure 10d) was located within an area of high footprint weight, relative to the two ends of the signal. This likely led to the anomalously high modeled $\overrightarrow{Q_{cr}}$ within a point-source region (Figure 10c) near the center of the measured signal in Figure 10d, and could have contributed to our underestimation of total leakage discharge based on $\overrightarrow{Q_{cr}}$. Given the challenges associated with the use of EC to detect, locate, and quantify CO_2 leakage signals of small magnitude and/or spatial extent within a background ecosystem, the application of EC in GCS monitoring programs should be guided by detailed site characterization, careful EC experiment design, and, ideally, the use of complementary measurement techniques.

Acknowledgements. We are grateful to five anonymous reviewers whose scrutiny and constructive comments greatly improved this paper. We thank J. Ajo-Franklin for careful review of the draft manuscript, K.Gullickson for assistance in the field and H.P. Schmid

for the FSAM source code. This work was funded by the ZERT Project, Assistant Secretary for Fossil Energy, Office of Sequestration, Hydrogen, and Clean Coal Fuels, NETL, of the U.S. Dept. of Energy under Contract No. DE-AC02-05CH11231.

References

Amiro, B.D. (1998), Footprint climatologies for evapotranspiration in a boreal catchment. *Agr. Forest Meteorol., 90*, 195–201.

Anderson, D.E. and C.D. Farrar (2001), Eddy covariance measurement of CO_2 flux to the atmosphere from an area of high volcanogenic emissions, Mammoth Mountain, California. *Chem. Geol., 177*, 31–42.

Aubinet, M., A. Grelle, A. Ibrom, et al. (2000), Estimates of the annual net carbon and water exchange of European forests: the EUROFLUX methodology. *Advan. Ecol. Res., 30*, 113–175.

Baldocchi, D.D. (2003), Assessing the eddy covariance technique for evaluating carbon dioxide exchange rates of ecosystems: past, present, and future. *Global Change Biol., 9*, 479–492.

Benson, S.M. (2006), Monitoring carbon dioxide sequestration in deep geological formations for inventory verification and carbon credits. *SPE Annual technical Conference*, San Antonio, TX, 24-27, September 2006.

Billesbach, D.P., M.L. Fischer, M.S. Torn, and J.A. Berry (2004), A portable eddy covariance system for the measurement of ecosystem-atmosphere exchange of CO_2, water vapor, and energy. *J. Atm. Ocean. Tech., 21*, 639–650.

Chiodini, G., G.R. Cioni, M. Guidi, B. Raco, and L. Marini (1998), Soil CO_2 flux measurements in volcanic and geothermal areas. *Appl. Geochem., 13*, 543–552.

Cortis, A., C.M. Oldenburg, and S.M. Benson (2008), The role of optimality in characterizing CO_2 seepage from geologic carbon sequestration sites. *Int. J. Greenhouse Gas Control*, *2*, 640–652.

Dahlen, F.A. and J. Tromp (1998), Theoretical Global Seismology. Princeton University Press, Princeton, NJ.

Falge, E., D.D. Baldocchi, R.J. Olson, et al. (2001), Gap filling strategies for defensible annual sums of net ecosystems exchange. *Agric. For. Meteorol. 107*, 43–69.

Fischer, M.L., D.P. Billesbach, J.A. Berry, R.J. Riley, and M.S. Torn (2007), Spatiotemporal variations in growing season exchanges of CO_2, H_2O, and sensible heat in agricultural fields of the southern Great Plains. *Earth Interact., 11*, 1–21.

Foken, T. and B. Wichura (1996), Tools for quality assessment of surface-based flux measurements. *Agric. For. Meteorol., 78*, 83–105.

Foken, T. and M.Y. Leclerc (2004), Methods and limitations in validation of footprint models. *Agric. For. Meteorol., 127*, 223–234.

Göckede, M. *et al.* (2008), Quality control of CarboEurope flux data – Part 1: footprint analyses with flux data quality assessment to evaluate sites in forest ecosystems. *Biogeosciences, 5*, 433–450.

Harris, R., and P. Segall (1987), Detection of a locked zone at depth on the Parkfield, California segment of the San Andreas fault. *J. Geophys. Res., 92*, 27945–27962.

Horst, T.W. and J.C. Weil (1992), Footprint estimation for scalar flux measurements in the atmospheric surface-layer. *Bound. Layer Meteorol., 59*, 279–296.

International Energy Agency (1997), Carbon Dioxide Utilization, IEA Greenhouse Gas R and D Programme, Paris.

International Energy Agency (2004), Prospects for CO_2 Capture and Storage, IEA Publications, Paris.

IPCC (2005), IPCC Special Report on Carbon Dioxide Capture and Storage, Cambridge University Press, Cambridge.

Kaimal, J.C. and J.J. Finnigan (1994), Atmospheric Boundary Layer Flows: Their Structure and Measurement. Oxford University Press, Oxford.

Leuning, R., D. Etheridge, A. Luhar, and B. Dunse (2008), Atmospheric monitoring and verification technologies for CO_2 geosequestration. *Int. J. Greenhouse Gas Control, 2*, 401–404.

Lewicki, J.L., G.E. Hilley, and C.M. Oldenburg (2005), An improved strategy to detect CO_2 leakage for verification of geologic carbon sequestration. *Geophys. Res. Lett., 32,* L19403, doi:10.1029/2005GL024281.

Lewicki, J.L., C.M. Oldenburg, L. Dobeck, L. and L. Spangler (2007), Surface CO_2 leakage during two shallow subsurface CO_2 releases. *Geophys. Res. Lett., 34*, L24402, doi:101029/2007GL032047.

Lewicki, J. L., M.L. Fischer, and G.E. Hilley (2008), Six-week time series of eddy covariance CO_2 flux at Mammoth Mountain, California: performance evaluation and role of meteorological forcing. *J. Volcanol. Geotherm. Res.,171*, 178–190.

Lloyd, J. and J.A.Taylor (1994), On the temperature-dependence of soil respiration. *Funct. Ecol., 8,* 315–323.

Massman, W.J. and X. Lee (2002), Eddy covariance flux corrections and uncertainties in long-term studies of carbon and energy exchanges. *Agric. For. Meteorol.,113,* 121–144.

Menke, W. (1989), Geophysical Data Analysis: Discrete Inverse Theory. Academic Press, San Diego.

Miles, N., K. Davis, and J. Wyngaard (2005), Detecting leaks from CO_2 reservoirs using micrometeorological methods, in Carbon Dioxide Capture for Storage in Deep Geologic Formations-Results From the CO_2 Capture Project, S. M. Benson, Ed. London, U.K.: Elsevier Science, 2005, vol. 2, *Geologic Storage of Carbon Dioxide With Monitoring and Verification*,1031–1044.

Oldenburg, C.M., J.L. Lewicki, and R.P. Hepple (2003), Near-surface monitoring strategies for carbon dioxide storage verification*, Lawrence Berkeley National Laboratory Report LBNL-54089*.

Reichstein, M., E. Falge, D. Baldocchi, et al. (2005), On the separation of net ecosystem exchange into assimilation and ecosystem respiration: review and improved algorithm, *Glob. Change Biol., 11*, 1424–1439.

Schmid, H.P. (1997), Experimental design for flux measurements: matching scales of observations and fluxes. *Agri. For. Meteorol., 87*, 179–200.

Webb, E.K., G.I. Pearman, and R. Leuning (1980), Correction of flux measurements for density effects due to heat and water vapour transfer. *Quart. J. Royal Meteorol. Soc., 106*, 85–100.

Werner, C., J.C. Wyngaard, and S.L. Brantley (2000), Eddy-correlation measurement of hydrothermal gases. *Geophys. Res. Lett., 27*, 2925–2928.

Werner, C., G. Chiodini, D. Voigt, S. Caliro, R. Avino, M. Russo, T. Brombach, J. Wyngaard, and S. Brantley (2003), Monitoring volcanic hazard using eddy covariance at Solfatara volcano, Naples, Italy. *Earth Planet. Sci. Lett., 210*, 561–577.

Table 1. Slow-response subsystem instrumentation and measurements.

Instrument	**Measured variable**
PTB101B barometer (Vaisala, Inc.)	Atmospheric pressure
HMP50 humidity and temperature probe (Vaisala, Inc.)	Atmospheric temperature and relative humidity
CS800-12 wind set (Climatronics Corp.)	Mean horizontal wind speed and direction
CNR-1 radiometer (Kipp & Zonen)	Net radiation
LI-200SA pyranometer (LI-COR)	Total insolation
LI-190SA quantum sensor (LI-COR)	Photosynthetically active radiation (PAR)
TE525 tipping bucket rain gage (Texas Electronics)	Cumulative precipitation
ECH2O soil moisture probe (Decagon Devices)	Relative soil moisture profiles
Thermocouples (in house)	Soil temperature profiles
HFT3 soil heat flux plates (Radiation and Energy Balance Systems)	Soil heat flux

Figure Captions

Figure 1. Schematic of the CO_2 release well at Montana State University. Gray zone is expanded to show example of a ~12 m perforated well zone from which CO_2 was released, bounded by two ~0.4 m inflatable packers.

Figure 2. Contour maps of log soil CO_2 flux for measurements made on (a) 7 July 2007 (background), (b) 16 July 2007 (Day 8 of Release 1), and (c) 10 August 2007 (Day 8 of Release 2). Dots show measurement locations. Black line and gray square in (a) show approximate locations of surface well trace and 2007 EC station, respectively. The 2006 EC station was located ~60 m north of the 2007 station.

Figure 3. Wind rose showing joint frequency distribution of mean horizontal wind speed and direction (half-hour averages) measured in 2006 and 2007.

Figure 4. Time series of (a) average daily atmospheric temperature (stars) and vapor pressure deficit (VPD; dots), (b) average daily PAR (dots) and relative soil moisture (stars), and (c) daily cumulative precipitation measured in 2006. Time series of (d) average daily atmospheric temperature (stars) and VPD (dots), (e) average daily PAR (dots) and relative soil moisture (stars), and (f) daily cumulative precipitation measured in 2007. Dashed vertical lines show timing of mowing of field. Gray zones show timing of Releases 1 and 2.

Figure 5. Half-hour F_c time series measured in (a) 2006 and (b) 2007. Dashed vertical lines show timing of mowing of the field. Gray zones show timing of Releases 1 and 2.

Figure 6. Histograms of (a) 2006 F_c, (b) 2007 F_c, (c) 2006 residual F_c (F_{cr}) after ecological flux filter applied, and (d) 2007 F_{cr} after ecological flux filter applied.

Figure 7. Upper 90th percentile residual F_c (F_{cr}) for seven-day moving window in 2006 (black dots) and 2007 (red dots). Black and red horizontal dashed lines show 90th percentile residual flux for an exhaustively sampled stationary Gaussian distributions with mean and standard deviation = 0 and 8.1 g m^{-2} d^{-1} (2006) and 0 and 9.3 g m^{-2} d^{-1} (2007), respectively. Vertical dashed lines show timing of 2006 and 2007 mowing. Gray zones show timing of Releases 1 and 2.

Figure 8. Radial plot of F_{cr} as a function of mean horizontal wind direction and time for 2007 data. Color bar denotes timing of measurements. Relatively large orange dots with black outlines are residuals measured during Release 2 (3-10 August 2007).

Figure 9. Plot of misfit between measured and modeled $\overrightarrow{F_{cr}}$ (as weighted residual sum of squares; WRSS) versus $\overrightarrow{Q_{cr}}$ roughness for different w_{sm}. A $w_{sm} = 10^{-8.5}$ was used in inversion.

Figure 10. Maps of (a) modeled surface CO_2 flux ($\overrightarrow{Q_{cr}}$) (note scale on color bar, where $Q_{cr} \geq 60$ and ≤ 0 g m^{-2} d^{-1} are dark red and blue, respectively), (b) footprint climatology

(contour map of sum of footprint weights based on 75 inverted footprint functions), and (c) modeled surface CO_2 flux shaded for uncertainty based on sum of footprint weights (b), where degree of masking increases with uncertainty. (d) Contour map color-coded for log soil CO_2 flux measured during Release 2 on 08/10/2007 (Figure 2c). White or black squares indicate location of EC station.

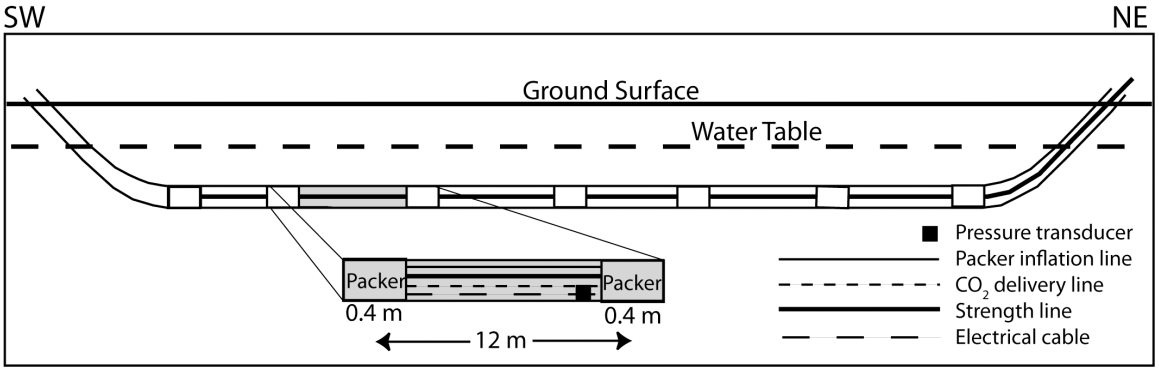
SW
NE
Ground Surface
Water Table
Packer
Packer
0.4 m
0.4 m
12 m
Pressure transducer
Packer inflation line
CO_2 delivery line
Strength line
Electrical cable

Figure 1

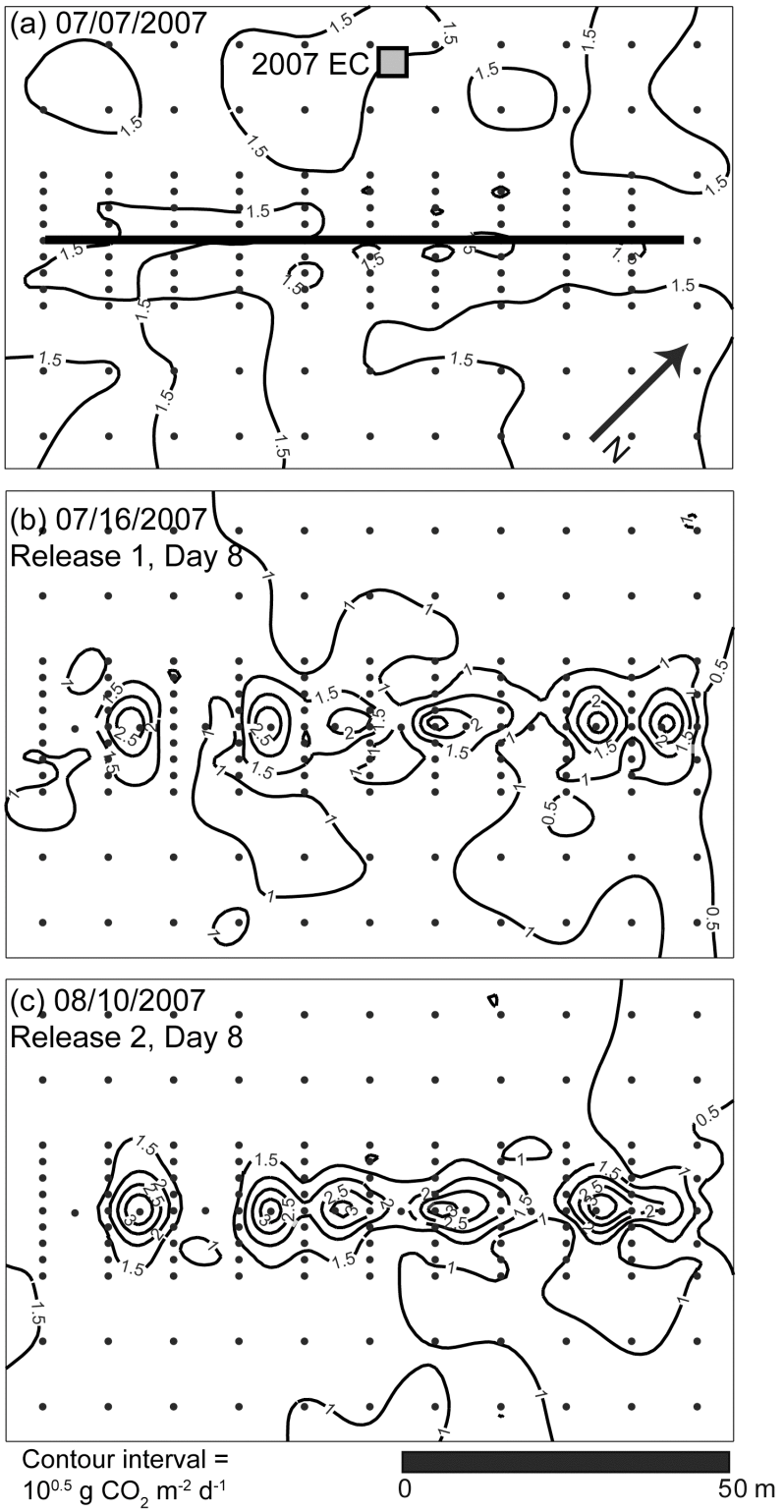
(a) 07/07/2007
2007 EC
N
(b) 07/16/2007
Release 1, Day 8
(c) 08/10/2007
Release 2, Day 8
Contour interval =
10^0.5 g CO2 m-2 d-1
0
50 m

Figure 2

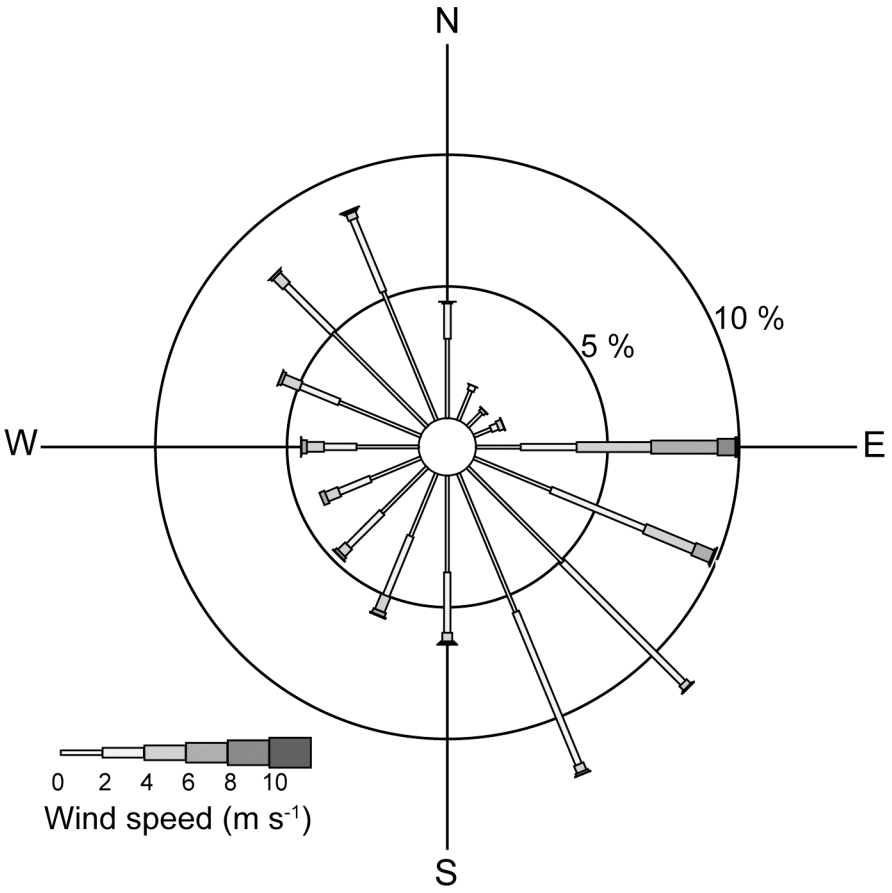

Figure 3

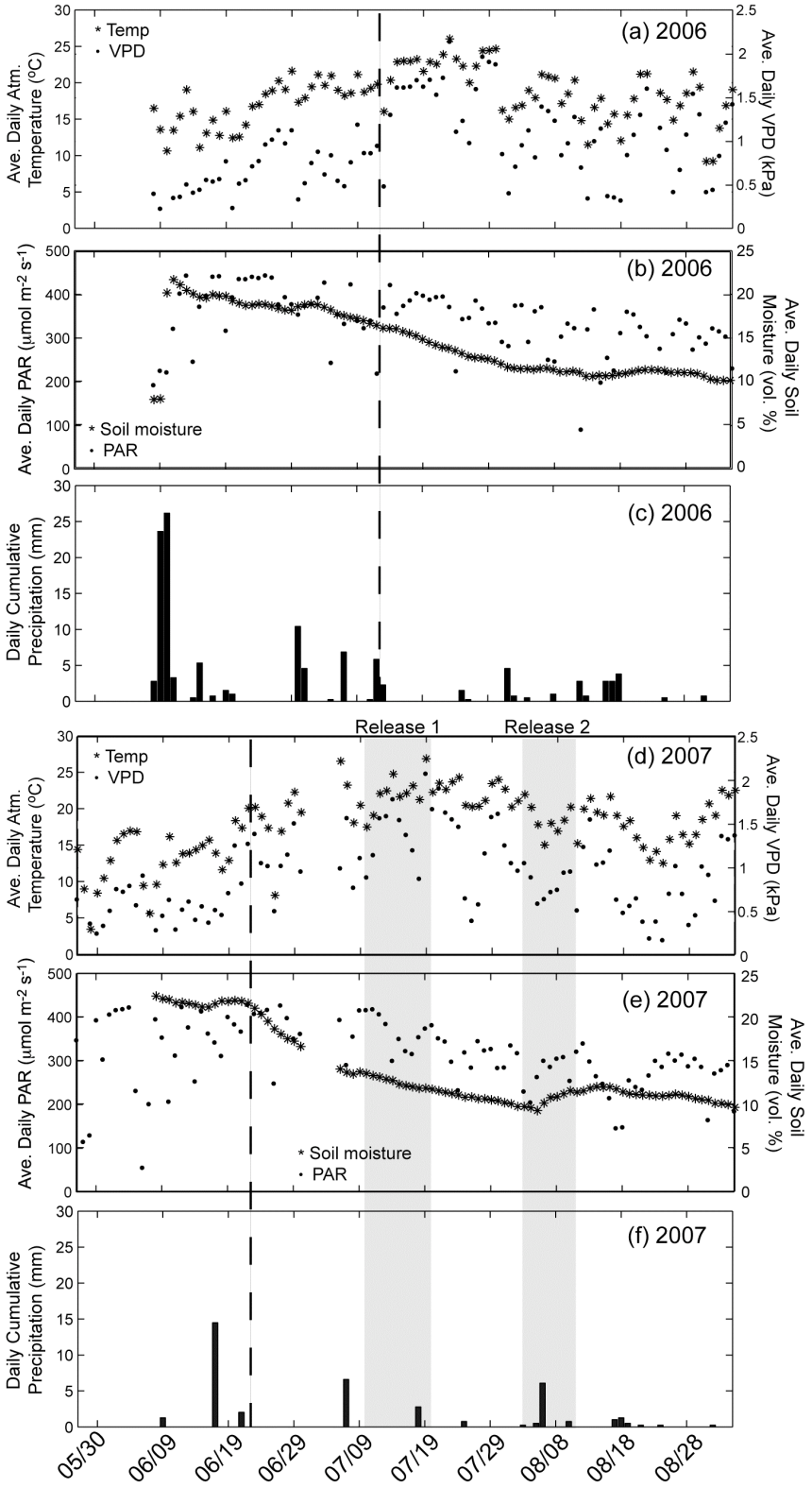
(a) 2006
Temp
VPD
Ave. Daily Atm. Temperature (°C)
Ave. Daily VPD (kPa)
(b) 2006
Soil moisture
PAR
Ave. Daily PAR (μmol m-2 s-1)
Ave. Daily Soil Moisture (vol. %)
(c) 2006
Daily Cumulative Precipitation (mm)
Release 1
Release 2
(d) 2007
(e) 2007
(f) 2007
05/30
06/09
06/19
06/29
07/09
07/19
07/29
08/08
08/18
08/28

Figure 4

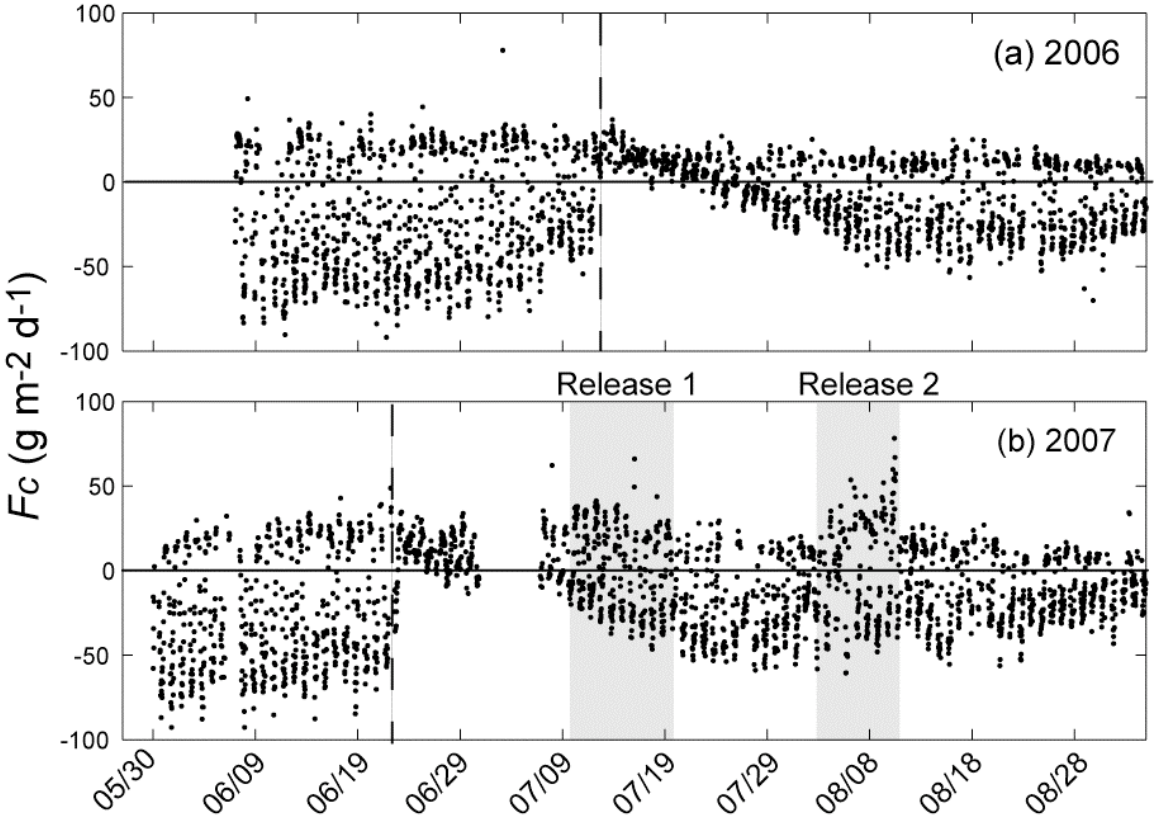
(a) 2006
(b) 2007
Release 1
Release 2
Fc (g m-2 d-1)
100
50
0
-50
-100
05/30
06/09
06/19
06/29
07/09
07/19
07/29
08/08
08/18
08/28

Figure 5

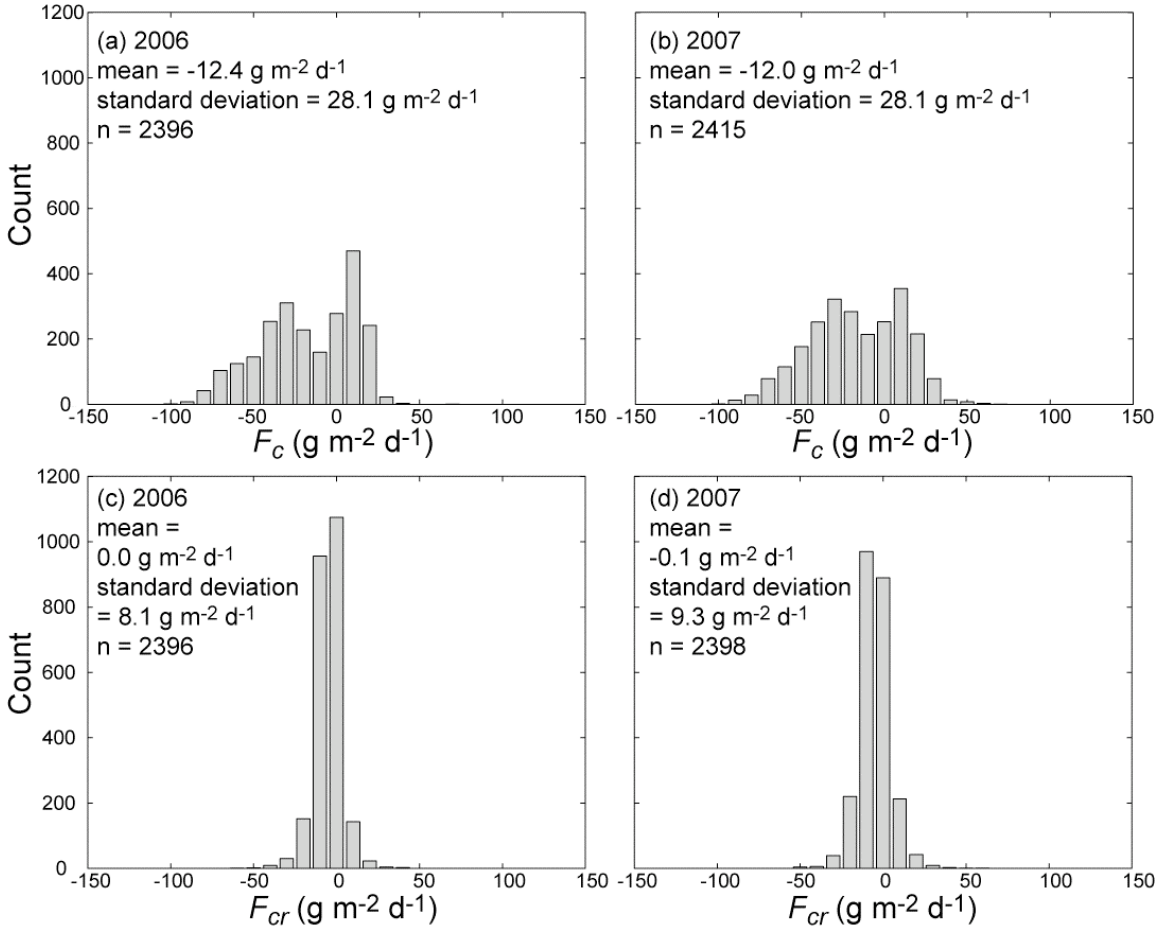
(a) 2006
mean = -12.4 g m-2 d-1
standard deviation = 28.1 g m-2 d-1
n = 2396
(b) 2007
mean = -12.0 g m-2 d-1
standard deviation = 28.1 g m-2 d-1
n = 2415
(c) 2006
mean =
0.0 g m-2 d-1
standard deviation
= 8.1 g m-2 d-1
n = 2396
(d) 2007
mean =
-0.1 g m-2 d-1
standard deviation
= 9.3 g m-2 d-1
n = 2398
Count
Fc (g m-2 d-1)
Fcr (g m-2 d-1)

Figure 6

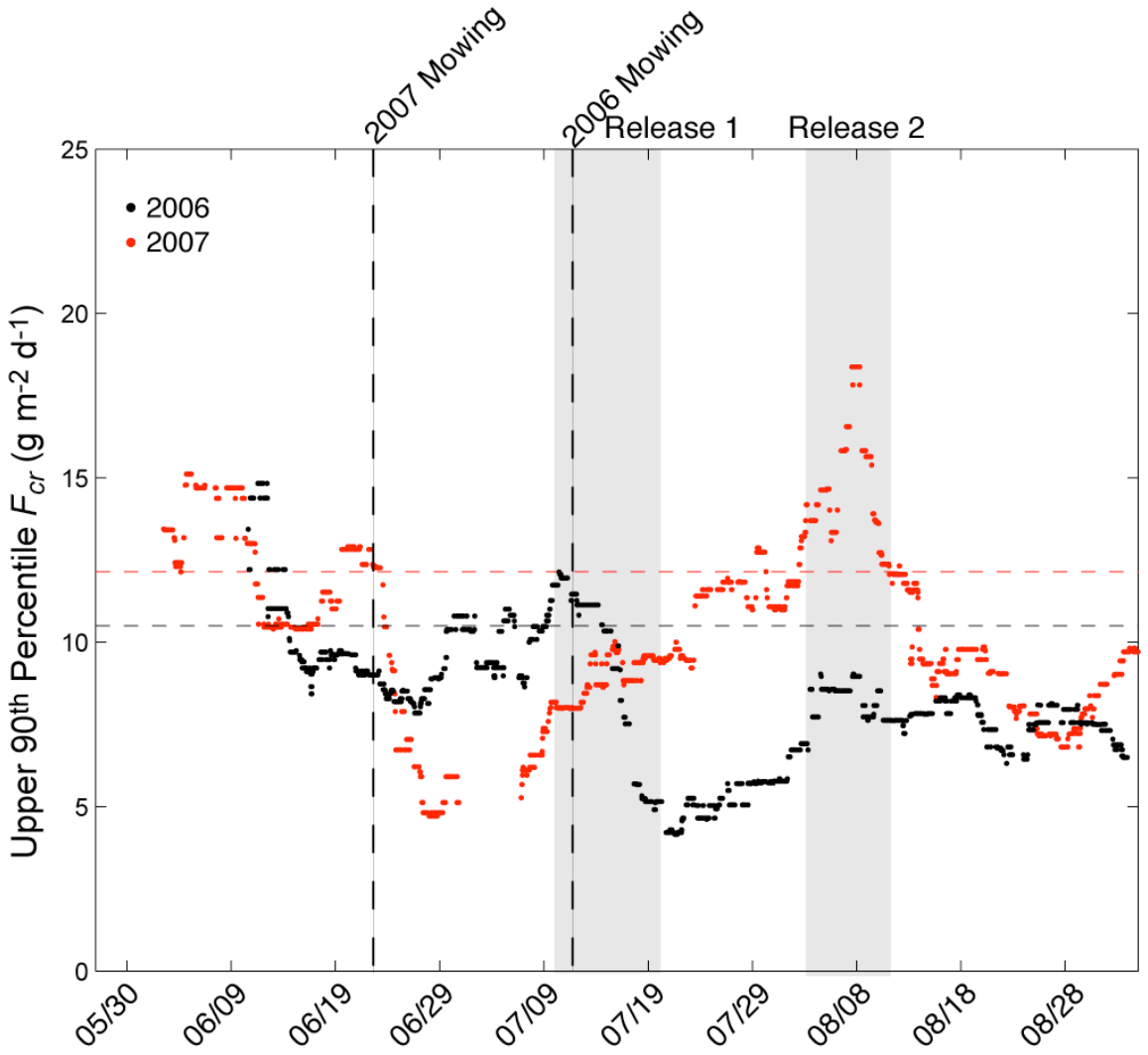
2007 Mowing
2006 Mowing
Release 1
Release 2
2006
2007
Upper 90th Percentile F_{cr} (g m-2 d-1)
25
20
15
10
5
0
05/30
06/09
06/19
06/29
07/09
07/19
07/29
08/08
08/18
08/28
Figure 7

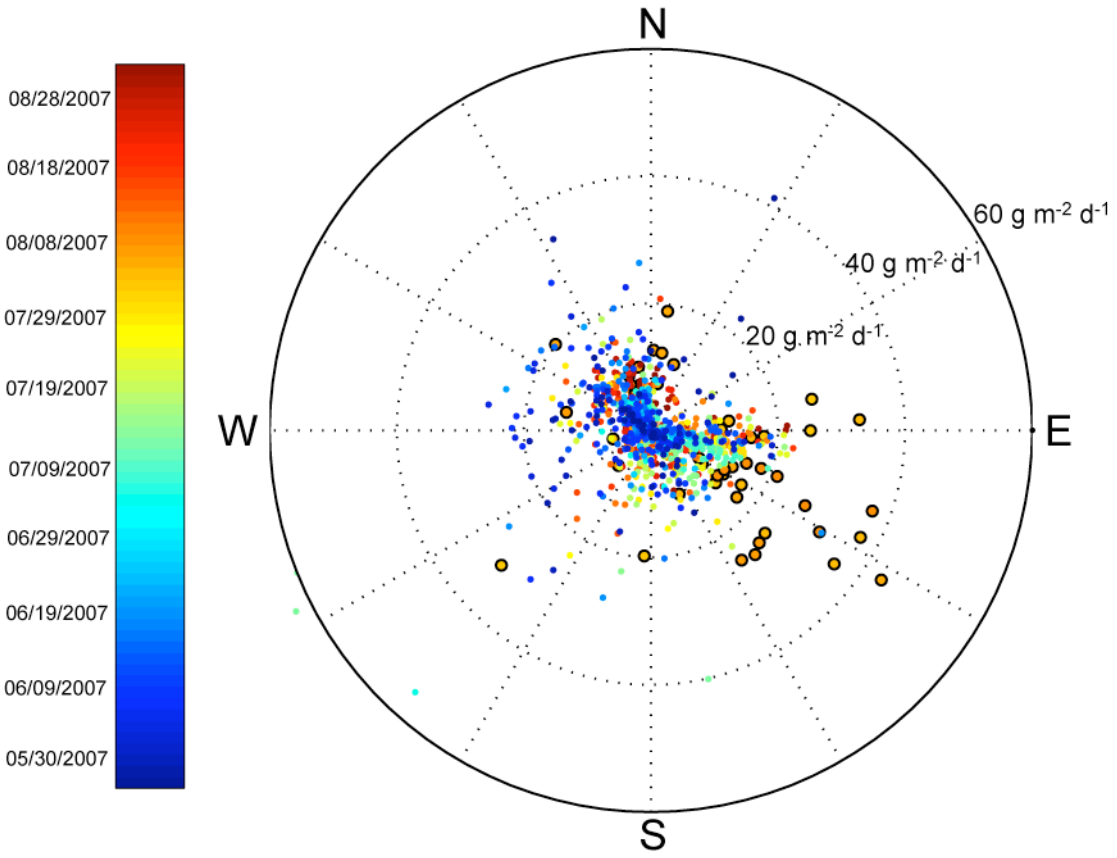
08/28/2007
08/18/2007
08/08/2007
07/29/2007
07/19/2007
07/09/2007
06/29/2007
06/19/2007
06/09/2007
05/30/2007
N
W
E
S
60 g m-2 d-1
40 g m-2 d-1
20 g m-2 d-1

Figure 8

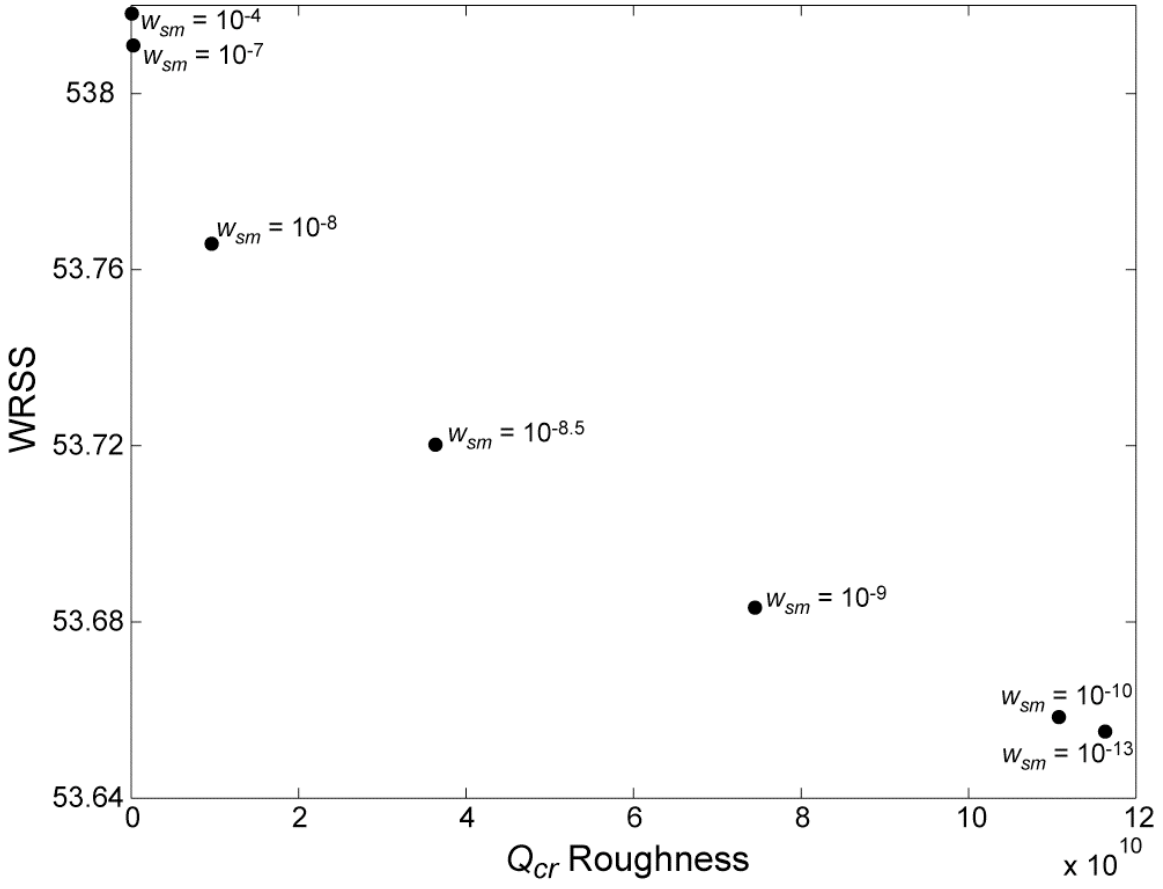
w_{sm} = 10^{-4}
w_{sm} = 10^{-7}
w_{sm} = 10^{-8}
w_{sm} = 10$^{-8.5}$
w_{sm} = 10^{-9}
w_{sm} = 10^{-10}
w_{sm} = 10^{-13}
538
53.76
53.72
53.68
53.64
WRSS
0
2
4
6
8
10
12
Q_{cr} Roughness
x 10^{10}

Figure 9

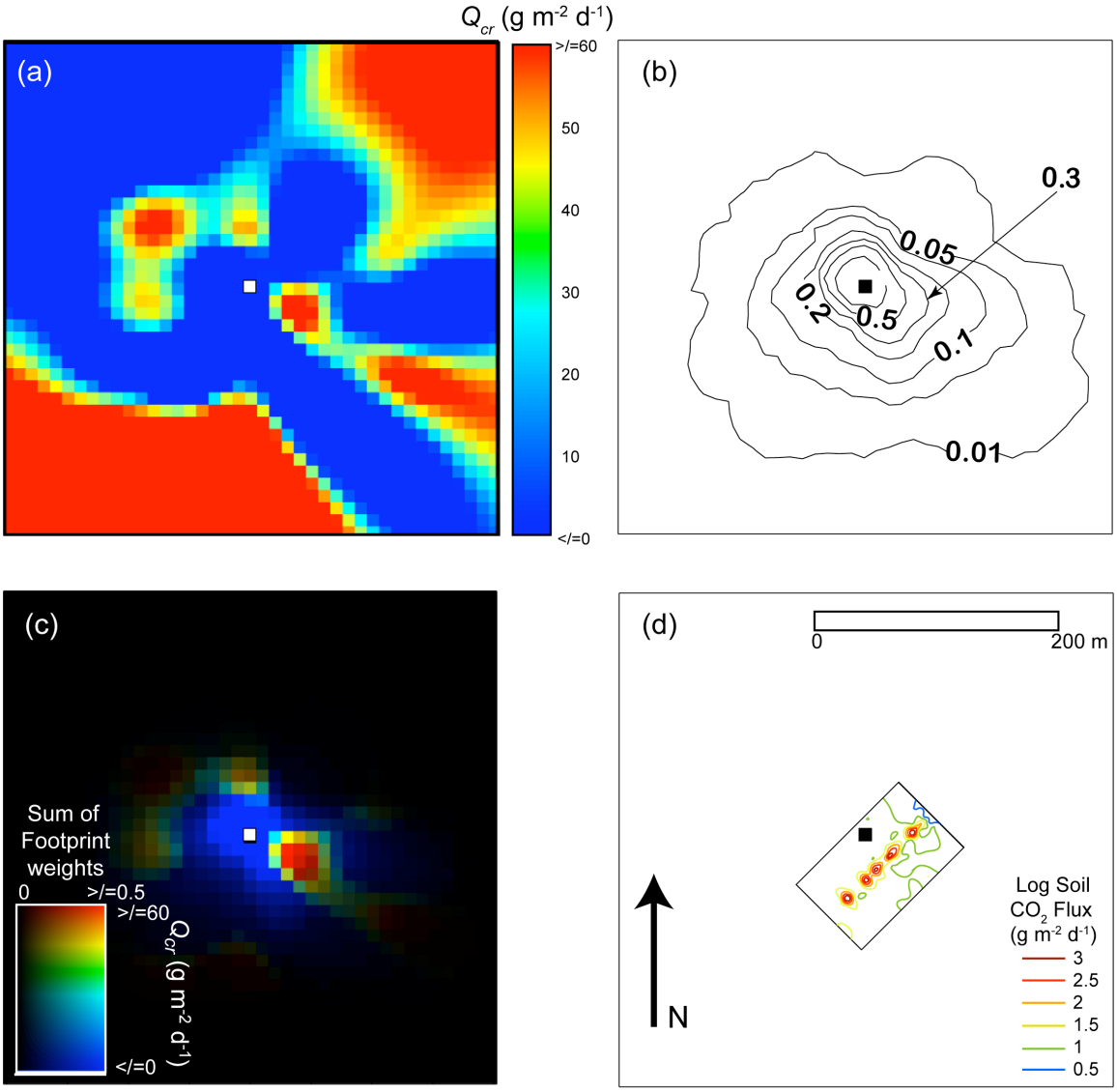
Q_{cr} (g m^{-2} d^{-1})
(a)
>/=60
50
40
30
20
10
</=0
(b)
0.3
0.05
0.2
0.5
0.1
0.01
(c)
Sum of Footprint weights
0
>/=0.5
>/=60
Q_{cr} (g m^{-2} d^{-1})
</=0
(d)
0
200 m
N
Log Soil CO_2 Flux (g m^{-2} d^{-1})
3
2.5
2
1.5
1
0.5

Figure 10